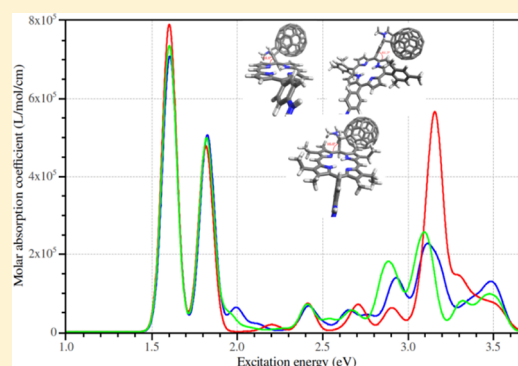


# Photoexcitation of Light-Harvesting C–P–C<sub>60</sub> Triads: A FLMO-TD-DFT Study

Junzi Liu, Yong Zhang, and Wenjian Liu\*

Beijing National Laboratory for Molecular Sciences, Institute of Theoretical and Computational Chemistry, State Key Laboratory of Rare Earth Materials Chemistry and Applications, College of Chemistry and Molecular Engineering, and Center for Computational Science and Engineering, Peking University, Beijing 100871, People's Republic of China

**ABSTRACT:** The recently proposed linear-scaling time-dependent density functional theory (TD-DFT) [*J. Chem. Theory. Comput.* **2011**, *7*, 3643] is employed to capture more than 300 low-lying excited states for three light-harvesting C–P–C<sub>60</sub> triads composed of  $\beta$ -carotenoid polyene (C), diaryl-based porphyrin (P), and pyrrole–fullerene (C<sub>60</sub>). The simulated optical absorption spectra are grossly in good agreement with experimental observations. To gain insights on the structure–property relations, both top-down and bottom-up analyses of the excited states are made in terms of the underlying fragment localized molecular orbitals (FLMO). A maximum occupation method is further proposed for finding excited-state solutions of self-consistent-field equations and is applied to long-range charge-transfer states that cannot be described by TD-DFT with pure density functionals.



## 1. INTRODUCTION

As the energy shortage is becoming a more and more serious issue, how to efficiently utilize solar energy has become a very hot topic of research in the last years.<sup>1</sup> Owing to light weights as well as good plasticity and processability, organic materials are highly favorable substitutes of silicon for photovoltaic devices. In this regard, polymer:fullerene bulk heterojunctions (BHJ) are particularly promising.<sup>2–6</sup> However, the energy conversion efficiency of BHJ solar cells is still quite low (ca. 10%)<sup>7</sup> compared with silicon-based ones. This results from several factors, including nanomorphology, exciton diffusion and dissociation at the interface of donor and acceptor, variability of molecular weights, polydispersity of  $\pi$ -conjugated polymers, residual end-group effect, and charge transportation.<sup>8,9</sup> Full optimizations of such factors are by no means trivial in fabricating efficient BHJ solar cells. Moreover, the complicated network structures of BHJ systems also plague the understanding of their structure–property relationships, such that a rational design is difficult, if not impossible. For this purpose, one should start with materials of well-defined structures, especially those in which the donor and acceptor are directly bonded.

It has been well-known that some light-harvesting natural products (e.g., chlorophylls and carotenoids) can exploit sunlight efficiently in photosynthesis. The photoinduced electronic excitations can undergo rapid charge separations so as to transform solar energy efficiently into electric potential energy. Inspired by this observation, many researchers investigated single molecular light-harvesting systems composed of porphyrin and fullerene (for a recent review, see ref 10), where the porphyrin unit serves as the photoreaction center and electron donor whereas fullerene serves as the

electron acceptor. For instance, Gust et al.<sup>11–13</sup> synthesized a series of C–P–C<sub>60</sub> triad molecules (Figure 1) that consist of a diaryl-based porphyrin (P) covalently bonded to  $\beta$ -carotenoid polyene (C) and pyrrole–fullerene (C<sub>60</sub>). It was found that such molecules can generate long-lived charge-separated states with reasonable quantum yields. Specifically, the first dipole-allowed excited singlet-state C–<sup>1</sup>P–C<sub>60</sub> localized on porphyrin undergoes ultrafast electron transfer to yield the charge-separated-state C–P<sup>•+</sup>–C<sub>60</sub><sup>•–</sup>, which eventually evolves to a long-lived charge-separated-state C<sup>•+</sup>–P–C<sub>60</sub><sup>•–</sup> via a rapid charge shift.<sup>13</sup> Except for such emission processes, the absorption spectra, to which photocurrent generation is directly related, also deserves attention. Recently, Pederson et al.<sup>14–16</sup> carried out both density functional theory (DFT) and (real-time) time-dependent DFT (TD-DFT) calculations on the basic triad shown in Figure 1 (I). Though some insights have been obtained on both the ground and excited states, a more comprehensive investigation on the photoexcitation spectra of the C–P–C<sub>60</sub> triads remains to be performed. It turns out that more than 300 excited states have to be captured to cover the visible part (1.55–3.10 eV) of the solar spectrum. This is quite challenging to any quantum chemical methods. Nevertheless, the linear-scaling TD-DFT developed recently by our group<sup>17</sup> has succeeded in capturing all the excited states below 3.55 eV. The results explain nicely the experimentally observed substitution effects<sup>13</sup> in the C–P–C<sub>60</sub> triads; i.e., *meso*-aryl substitutions [Figure 1 (II)] tend to have a higher electron-transfer efficiency than  $\beta$ -alkyl substitutions [Figure 1 (III)].

Received: January 29, 2014

Published: May 5, 2014

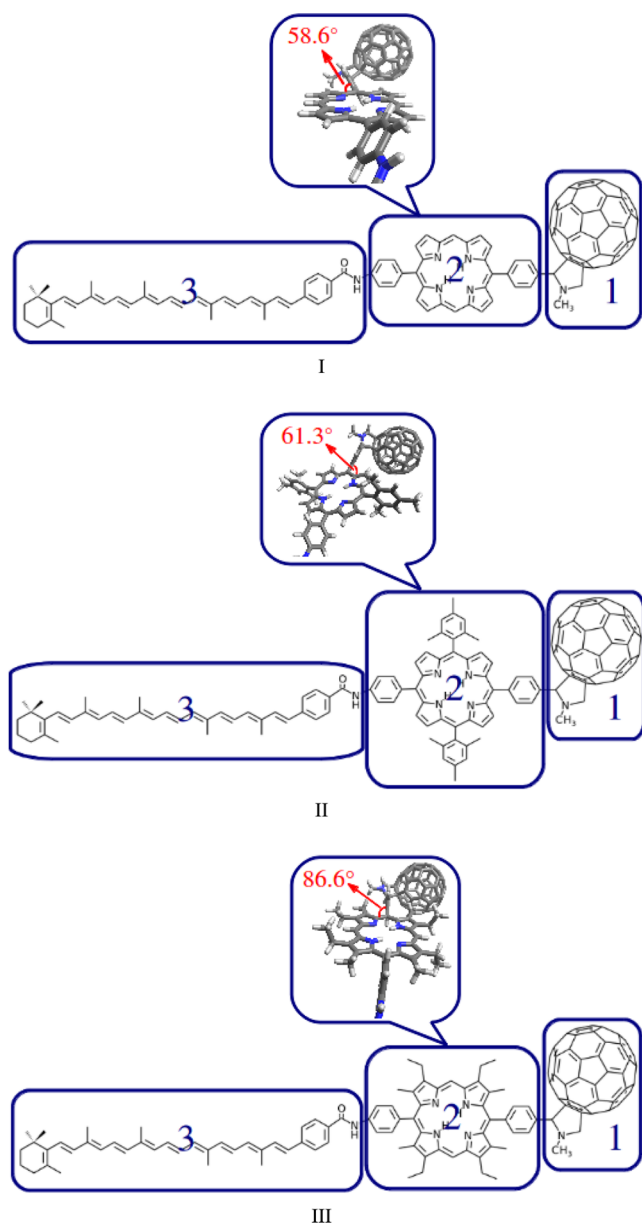


Figure 1. Optimized structures for the C-P-C<sub>60</sub> triads.

## 2. THEORETICAL METHODS

**2.1. FLMO-TD-DFT.** In the linear response regime, TD-DFT in the frequency domain amounts to solving the following generalized eigenvalue equation:<sup>18</sup>

$$\begin{pmatrix} \mathbf{A} & \mathbf{B} \\ \mathbf{B} & \mathbf{A} \end{pmatrix} \begin{pmatrix} \mathbf{X} \\ \mathbf{Y} \end{pmatrix} = \begin{pmatrix} \mathbf{I} & \mathbf{O} \\ \mathbf{O} & -\mathbf{I} \end{pmatrix} \begin{pmatrix} \mathbf{X} \\ \mathbf{Y} \end{pmatrix} \omega \quad (1)$$

$$A_{ai,bj} = \Delta_{ai,bj} + K_{ai,bj} \quad (2)$$

$$B_{ai,bj} = K_{ai,jb} \quad (3)$$

$$\Delta_{ai,bj} = \delta_{ij} f_{ab} - \delta_{ab} f_{ji} \quad (4)$$

$$K_{ai,bj} = (a|ljb) + (a|l f_{xc} |jb) \quad (5)$$

Here, the indices  $\{i, j\}$  and  $\{a, b\}$  denote the occupied (hole) and virtual (particle) orbitals, respectively. Under the adiabatic approximation, the exchange–correlation (XC) kernel  $f_{xc}$  is just

the second-order derivative of the XC energy functional  $E_{xc}$  with respect to the (spin) density, such that the left-hand side of eq 1 is frequency independent. That is, eq 1 can in principle be solved by a single diagonalization. The cost would be of  $O(N_{ph}^3)$ , with  $N_{ph}$  being the product of the numbers of the occupied ( $N_o$ ) and virtual ( $N_v$ ) orbitals. In other words, such a one-step diagonalization would scale roughly as  $O(N^6)$ , with  $N$  being the characteristic size of the system. In practice, only a few low-lying excited states are of interest, which can be obtained more efficiently by solving eq 1 in an iterative manner. It turns out that, among the Krylov subspace iterative methods,<sup>19</sup> the modified Davidson iterative scheme<sup>20</sup> is most robust for solving the reduced form of eq 1

$$(\mathbf{A} - \mathbf{B})(\mathbf{A} + \mathbf{B})|\mathbf{R}_i\rangle = \omega_i^2|\mathbf{R}_i\rangle \quad |\mathbf{R}_i\rangle = |\mathbf{X}_i + \mathbf{Y}_i\rangle \quad (6)$$

Note in passing that  $\langle \mathbf{L}_i | = \langle \mathbf{X}_i - \mathbf{Y}_i |$ , subject to the biorthogonal conditions  $\langle \mathbf{L}_k | \mathbf{R}_l \rangle = \delta_{kl}$  are the left eigenvectors of eq 6.

Noticeably, the robustness of the subspace iterative schemes is only observed in the CMO (canonical molecular orbital) representation, where the quantity  $\Delta$  (4) is diagonal [i.e.,  $\Delta_{ai,bj} = (\epsilon_a - \epsilon_i)\delta_{ij}\delta_{ab}$ ] and dominates over the coupling term  $K$  (5). It is well-known that the CMOs are usually delocalized through the whole space, such that every particle–hole (p–h) pair contributes a little but cannot be truncated, thereby leading to a very dense coupling matrix  $K$  (5). The computational cost is then  $O(N^3)$  and is still very expensive for large systems. The only way to make  $K$  sparse is to go to a local representation. The atom-centered atomic orbitals (AO) are by definition most local in space. However, they are most “delocalized in energy”,<sup>17</sup> manifested by the large off-diagonal blocks of  $\Delta$ . This is in contrast with the CMOs which are “local in energy but delocalized in space”. What are in between are the localized molecular orbitals (LMOs), which may have good localities both in energy and in space. The crucial issue is then how to construct the desired occupied and virtual LMOs for large molecular systems composed of any kind of chemical bonds and described by any kind of basis functions. As shown by Jansík et al.,<sup>21,22</sup> this can indeed be achieved by a trust region minimization of powers of the orbital variance. At variance with such a top-down scheme, we recently proposed a bottom-up procedure based on the idea of “from fragments to molecule”.<sup>17,24</sup> It involves the following steps:

- (1) Divide the entire system into fragments according to chemical intuition.
- (2) Cap each fragment with parts of the system that are directly bonded to the fragment.
- (3) Saturate the dangling bonds with link atoms to form closed subsystems.
- (4) Carry out standard self-consistent-field (SCF) calculation for each subsystem.
- (5) Localize the CMOs for each subsystem with the standard Boys scheme.<sup>23</sup>
- (6) Pick up only those LMOs centered on the fragments according to the Löwdin population.
- (7) Project out the basis functions of the link atoms because these atoms are not part of the entire system.
- (8) Symmetrically orthonormalize the resulting linearly independent LMOs to form “primitive fragment LMO” (pFLMO).
- (9) Take the pFLMOs as the basis for the SCF calculation of the entire system.

Table 1. Computational Statistics<sup>a</sup>

	triad I C <sub>133</sub> H <sub>72</sub> N <sub>6</sub> O	triad II C <sub>151</sub> H <sub>92</sub> N <sub>6</sub> O	triad III C <sub>145</sub> H <sub>96</sub> N <sub>6</sub> O
N <sub>A</sub>	212	250	248
N <sub>o</sub>	460(320)	524(366)	508(356)
N <sub>v</sub>	2632(2492)	3030(2872)	2954(2802)
N <sub>ph</sub>	1210720(797440)	1587720(1051152)	1500632(997512)
N <sub>eff</sub> (η = 6)	18 282	18 100	17 707
(N <sub>eff</sub> /N <sub>ph</sub> ) × 100 (η = 6)	1.5(2.3)	1.1(1.7)	1.2(1.8)
N <sub>eff</sub> (η = 5)	5296	5119	5051
(N <sub>eff</sub> /N <sub>ph</sub> ) × 100 (η = 5)	0.4(0.7)	0.3(0.5)	0.3(0.5)

<sup>a</sup>N<sub>A</sub>: number of atoms. The numbers of occupied (N<sub>o</sub>) and virtual (N<sub>v</sub>) orbitals employed in FLMO-TD-DFT are in parentheses. N<sub>ph</sub> = N<sub>o</sub>N<sub>v</sub>. N<sub>eff</sub>: number of effective p–h pairs.

- (10) Construct noniteratively the global CMO to LMO unitary transformations  $\mathbf{U}_{oo}$  and  $\mathbf{U}_{vv}$  for the occupied and virtual spaces, respectively (see Appendix A of ref 17).

At first glance, the above procedure is quite involved. However, this is not really the case. Because of the conquering step (9), the dividing steps (1–3) can actually be arbitrary, with no particular limits on the size or kind of the fragments and buffers. It is just that the fragments are more transferable if they better respect the local chemical bondings. The subsystem calculations (4–7) can obviously be carried out on parallel computer nodes, such that only the timing of the largest subsystem counts. The computational overhead for steps (1–8) to generate the pFLMOs is overcompensated by the reduced number of iterations in the global SCF calculation (9), because the superposition of the fragments provides a much better initial guess than the superposition of atoms. After the global SCF has converged, the localization step (10) is essentially free of cost, e.g., it takes only 2 s for 1210 basis functions (for more details see Table 2 of ref 17). The resulting LMOs are orthonormal and well localized on the parent fragments. For this reason, they have been termed “fragment LMO” (FLMO). In sum, the success of this bottom-up localization procedure is ensured by the good transferability of the fragments on one hand, and by the particular block-diagonalization that leads to least changes in the occupied–occupied and virtual–virtual diagonal blocks of the Hartree–Fock/Kohn–Sham matrix on the other. As both the orbital picture and the integral number of electrons are retained, the nature of the excitations, whether local, delocalized, or charge transfer (CT), can readily be deduced from analysis of the excited-state eigenvectors in terms of transitions between fragments.

To expedite the prescreening of the FLMO p–h pairs, we introduce a parameter  $\eta_{ai}^B$  to measure the significance of the *ai* pair for a given batch *B* of grid points:

$$\eta_{ai}^B = -\log O_{ai}^B \quad \eta_{ai}^B \in [0, +\infty) \quad (7)$$

$$O_{ai}^B = \sum_{p \in B} w(\vec{r}_p) |\varphi_a(\vec{r}_p) \varphi_i(\vec{r}_p)| \quad O_{ai}^B \in [0, 1] \quad (8)$$

Here,  $w(\vec{r}_p)$  are the weights of the grid points. The larger the distance between the p–h pair *ai* and the grid batch *B* or the distance between the orbitals  $\varphi_a$  and  $\varphi_i$ , the smaller the  $O_{ai}^B$  and, hence, the larger the  $\eta_{ai}^B$ . All the FLMO p–h pairs will be screened out if their  $\eta_{ai}^B$  are larger than a preset threshold  $\eta$ . It was found<sup>17</sup> empirically that the accuracy in the excitation energies is ca.  $10^{-\eta+3}$  eV. That is, a value of 6 for  $\eta$  is usually

sufficient. With this simple prescreening, the number of effective FLMO p–h pairs (typically 1–2% of the total pairs, Table 1) scales linearly with the molecular size. The computationally expensive steps, including the induced density and Coulomb potential as well as the contraction between the coupling matrix **K** and the trial vector **b**, then become linear scaling. To explore the energetic locality of CMOs, the contracted product **Kb** is back-transformed to the CMO space. This step scales as  $O(N^3)$  but with a very small prefactor. The overall scaling of FLMO-TD-DFT is still  $O(N)$  with a very early crossover point. In case too many excited states are to be targeted, they can be split into batches. Subsequent states can be found by shifting the calculated interior states outside the spectrum. This amounts to rewriting eq 6 as

$$[(\mathbf{A} - \mathbf{B})(\mathbf{A} + \mathbf{B}) + \lambda \sum_i |\mathbf{R}_i\rangle\langle\mathbf{L}_i|] |\mathbf{R}_j\rangle = \omega_j^2 |\mathbf{R}_j\rangle \quad (9)$$

$$\lambda = (\epsilon_a^{\max} - \epsilon_i^{\min})^2 + \lambda_c \quad (10)$$

where  $\epsilon_a^{\max}$  and  $\epsilon_i^{\min}$  are the respective energy levels of the highest virtual and lowest occupied orbital and  $\lambda_c$  is an appropriate positive-valued constant.

At this stage, brief comparisons between the present FLMO-TD-DFT and other efficient implementations of TD-DFT should be made. In the absence of diffuse functions, the efficiencies of FLMO-TD-DFT and AO-TD-DFT<sup>25,26</sup> are comparable. However, in the presence of diffuse basis functions, LMO-TD-DFT becomes more efficient than AO-TD-DFT, because the cutoff of AO pairs becomes ineffective whereas the LMO p–h pairs can still be significantly cut off. The state-selective TD-DFT<sup>27</sup> is formally more efficient than both FLMO-TD-DFT and AO-TD-DFT. However, the goal there is to only calculate some predesignated states. The approach requires some a priori knowledge on the target states and the elimination of the artificially low-lying long-range CT p–h pairs is not really effective (vide post), except for systems composed of weakly interacting units. The most efficient implementation of TD-DFT is probably the simplified Tamm–Dancoff approximation (sTDA).<sup>28</sup> Yet, its efficiency stems primarily from a simple atom-centered monopole type of approximation for the four-index two-electron repulsion integrals in the CMO basis. In contrast, the efficacy of the perturbative selection of important p–h pairs employed therein is very much the same as the present prescreening scheme. For instance, if  $\eta = 5$  is chosen for the cutoff threshold, which implies an error of ca. 0.01 eV for the excitation energies, the surviving effective p–h pairs are only 0.5% of the total pairs (Table 1). This is



comparable with that of sTDA with a tolerance of 0.05 eV for the excitation energies.<sup>28</sup> At variance with such standard TD-DFT (TDA) that calculates the excitation energies of both bright and dark states from the eigenvalue problem (1), there also exists a variant of TD-DFT that calculates the damped linear response function, from which the excitation energies of bright states can be extracted a posteriori. Here, one can mention two kinds of implementations, the one<sup>29</sup> that can calculate any part of the spectrum and the one<sup>30</sup> that calculates, by construction, the entire spectrum at once. Yet, the former has not yet been made linear scaling, whereas the latter has to be combined with pseudopotentials to truncate the spectrum of the Hamiltonian and does not provide detailed information on individual excited states. Except for computational efficiency, an easy and pictorial interpretation of the excited states is also desired. In this regard, the present FLMO-TD-DFT is clearly advantageous.

**2.2. Maximum Occupation Method.** It is well-known that TD-DFT under the adiabatic local density approximation (ALDA) of the XC kernel cannot describe long-range CT states, due to the so-called “charge-transfer self-interaction error”.<sup>31</sup> They are thus often eliminated<sup>27</sup> from the outset by using, e.g., the orbital-density-based overlap

$$\tau_{ai} = \langle |\varphi_a|^2 || \varphi_i|^2 \rangle \quad (11)$$

as a criterion.<sup>32</sup> However, such states can well be described even with ALDA/TD-DFT if the electronic Hessian is revised to include some higher order terms.<sup>33</sup> An alternative remedy is to use a long-range corrected functional that becomes pure Hartree–Fock exchange in the long range.<sup>34–36</sup> Instead of these kinds of remedies to TD-DFT, we here propose a self-consistent maximum occupation method (mom) for handling the long-range CT states dominated by a single p–h pair. At variance with the constricted variational DFT,<sup>37,38</sup> the orthogonality between the excited and ground states is abandoned here. As a matter of fact, the present mom is just a simple but important revision of the original maximum overlap method (MOM) developed by Gilbert<sup>39</sup> for finding excited-state solutions of SCF equations. Instead of using the Aufbau principle, Gilbert showed that an excited state can be calculated variationally by occupying in each SCF iteration those orbitals that overlap most with the prechosen occupied space  $\{\tilde{\varphi}_i\}_{i=1}^N$ . Specifically, the  $N$  occupied spin orbitals  $\{\varphi_j\}_{j=1}^N$  are determined according to the largest projections  $P_j$

$$P_j = \sum_i^N C_{ij} \quad C_{ij} = \langle \tilde{\varphi}_i | \varphi_j \rangle \quad (12)$$

However, this selection of the occupied orbitals  $\{\varphi_j\}_{j=1}^N$  may not always work. First, every orbital  $\varphi_j$  should be in phase with all the  $\tilde{\varphi}_i$  (i.e.,  $C_{ij} \geq 0 \forall i$ ), which is difficult to fulfill in general. Second, in case a number of  $\tilde{\varphi}_i$  are nearly degenerate, a wrong orbital  $\varphi_j$  may actually be chosen: It has a *large* projection  $P_j$  but should *not* be chosen as occupied. To see this, we write the orbital  $\varphi_j$  as

$$|\varphi_j\rangle = \sum_i^N |\tilde{\varphi}_i\rangle C_{ij} + \sum_{a=N+1}^N |\tilde{\varphi}_a\rangle C_{aj} \quad (13)$$

where  $\{\tilde{\varphi}_a\}$  are the initial virtual orbitals. Imagine two orbitals  $\varphi_j$  and  $\varphi_k$ , the former being dominated by a single contribution from  $\tilde{\varphi}_i$  (i.e.,  $P_j \approx C_{ij} \approx 1$ ) and the latter being a heavy mixture of  $m_l$  nearly degenerate orbitals  $\tilde{\varphi}_l$  (i.e.,  $C_{lk}$  are all small). It is

very possible that  $P_j \approx 1$  is smaller than  $P_k = \sum_l^m C_{lk}$  but it is  $\varphi_j$  instead of  $\varphi_k$  that should be chosen as the desired occupied orbital. To remedy both defects, we introduce the orbital occupation  $n_j$  of orbital  $\varphi_j$  in the occupied space, viz.,

$$n_j = \sum_i^N |C_{ij}|^2 = \langle \varphi_j | P_0 | \varphi_j \rangle \quad P_0 = \sum_i^N |\tilde{\varphi}_i\rangle \langle \tilde{\varphi}_i| \quad (14)$$

The occupied orbitals  $\{\varphi_j\}_{j=1}^N$  are then chosen in each SCF iteration according to the largest occupations  $n_j$ . It has been verified that the present mom and the original MOM lead to the same results for molecules with simple orbital spectra. However, the present mom should be used for systems with dense energy levels.

Due to the loss of orthogonality, the transition dipole moment  $\vec{\mu}$  between the ground-state  $|0\rangle$  and an excited-state  $|I\rangle$  should be calculated as

$$\vec{\mu} = -\langle 0 | \vec{r} | I \rangle = -D_{0I} \sum_{ij}^N \langle \tilde{\varphi}_i | \vec{r} | \varphi_j \rangle (C^{-1})_{ji} \quad (15)$$

where  $D_{0I}$  is the determinant of matrix  $C$  (12) and can be used to check to what extent the  $|0\rangle$  and  $|I\rangle$  states overlap. The oscillator strength  $f_I$  can then be calculated as

$$f_I = \frac{2}{3} (E_I - E_0) (\mu_x^2 + \mu_y^2 + \mu_z^2) \quad (16)$$

Apart from the loss of strict orthogonality, the mom/MOM is of great advantage in several aspects:<sup>39</sup> (1) Analytic derivatives can readily be implemented for geometry optimizations of excited states. (2) Not only singly but also multiply excited states can be handled. (3) Wave-function-based correlation methods can be applied to excited states in the same way as to ground states.

### 3. COMPUTATIONAL DETAILS

The geometries of the three molecules (cf. Figure 1) were fully optimized with the PBE<sup>40</sup> parametrization of the generalized-gradient approximation (GGA) and a Slater-type DZP basis set.<sup>41</sup> Then, single point calculations were carried out with the SAOP (statistically averaging of model orbital potentials) XC potential<sup>42</sup> and a Slater-type TZP basis set. Unlike the XC potentials of standard GGA functionals, the SAOP potential has, by construction, the correct long-range behavior. The VWN5 form<sup>43</sup> of the local density approximation (LDA) was employed for the XC kernel of FLMO-TD-DFT. Although the SCF and FLMO-TD-DFT calculations can in principle adopt different fragmentations, we consider here a unified fragmentation as shown in Figure 1. This fragmentation appears natural for the HOMO (highest occupied MO) and LUMO (lowest unoccupied MO) are localized on the  $\beta$ -carotenoid polyene and pyrrole–fullerene, respectively. All the calculations were performed with the BDF program package.<sup>44–46</sup>

### 4. RESULTS AND DISCUSSION

**4.1. Ground-State Electronic Structure.** The Gaussian broadened densities of states (DOS) for the three triads are plotted in Figure 2 by using the Multiwfn3.0 software.<sup>47</sup> It is seen that the DOS of the three triads are very much the same between  $-9.0$  and  $-7.2$  eV, covering the HOMO–3 to LUMO +3 orbitals. Actually, the DOS of triads I and II are very similar for the entire range of energy, particularly between  $-9.4$  and  $-5.6$  eV covering the HOMO–7 to LUMO+17 orbitals. In

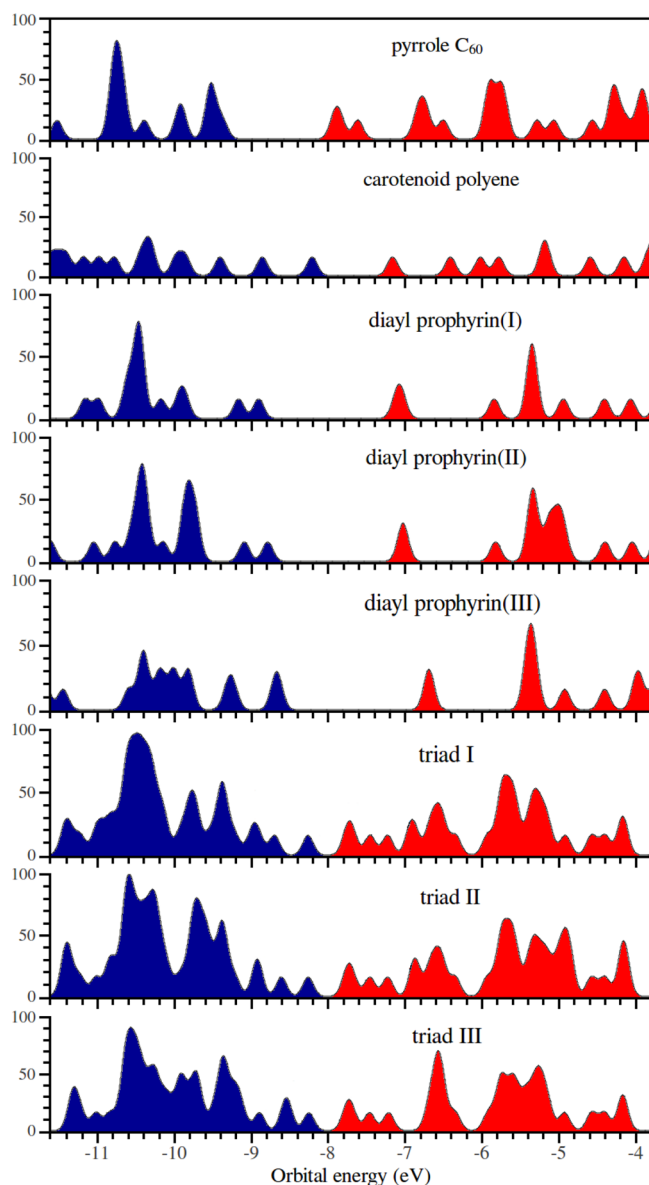


**Figure 2.** Gaussian broadened [full width at half-maximum (fwhm) = 0.15 eV] densities of states for the fragments and triads.

contrast, the DOS of triad III appears quite different from the other two below  $-9.0$  eV and above  $-7.2$  eV. These findings indicate that the *meso*-aryl substitutions of porphyrin [Figure 1 (II)] have little effect on the electronic structure of triad I, as compared with the  $\beta$ -alkyl substitutions [Figure 1 (III)]. This can be understood in terms of the local structures: The dihedral angle between the porphyrin and the linking benzene rings is ca.  $60^\circ$  for both triads I and II (specifically,  $58.6^\circ$  vs  $61.3^\circ$ ) but becomes  $86.6^\circ$  for triad III. That is, due to steric repulsion, the  $\beta$ -alkyl substitutions render the two benzene rings of triad III almost parallel but perpendicular to the porphyrin, so as to hinder the macrocyclic conjugation.

To gain more insights into the electronic structure, the frontier orbitals of the triads and fragments are further given in Table 2. Here, the fragments refer to parts of the triad (cf. Figure 1) that are geometrically not relaxed but are saturated with hydrogen atoms. That is, any possible changes going from such fragments to the triad reflect merely electronic redistributions and delocalizations. For convenience, we shall call the  $\beta$ -carotenoid polyene, diary-based porphyrin and pyrrole–fullerene units simply as carotenoid, porphyrin, and fullerene, respectively. It is seen that the HOMO, LUMO, LUMO+1, and LUMO+2 of the three triads have the same origin, viz., the HOMO of carotenoid and the LUMO, LUMO+1, and LUMO+2 of fullerene, respectively. As such, they share the same HOMO–LUMO gap of 0.5 eV [NB: The LDA/GGA gap is ca. 0.15 eV<sup>14,15</sup>]. These virtual orbitals arise from the pyrrole splitting of the triply degenerate  $t_{1u}$  LUMO of the isolated  $C_{60}$ . More interesting are the frontier orbitals of the porphyrin units. It is seen that the HOMO–LUMO gap of porphyrin in triads I and II is ca. 1.75 eV but increases to 1.95 eV in triad III. Moreover, the HOMO–1 of porphyrin in triads I and II is lower than the HOMO (and the HOMO–1 of carotenoid) by ca. 0.3 eV, but that in triad III is nearly degenerate with the HOMO and even higher than the HOMO–1 of carotenoid. When the triads form, the HOMO of porphyrin becomes the HOMO–1 of the triads, with the energy increased by ca. 0.2 eV in the case of triads I and II, but by only 0.1 eV in the case of triad III. The same situation occurs also to the HOMO–1 of porphyrin, which corresponds to the HOMO–3 of the triads. As for the low-lying virtual orbitals of porphyrin, it is seen that the nearly degenerate LUMO and LUMO+1 of porphyrin are lower in the case of triads I and II but become higher in the case of triad III, by ca. 0.2 eV than the

**Table 2.** Energy Levels (eV) of the Triads and Their Constituent Fragments<sup>a</sup>

triad I		fragment		triad II		fragment		triad III		fragment	
L7	−6.62	L4[1]	−6.77	L7	−6.62	L4[1]	−6.84	L5	−6.62	L4[1]	−6.77
L6	−6.68	L3[1]	−6.84	L6	−6.69	L3[1]	−6.84	L4	−6.69	L3[1]	−6.84
L5	−6.87	L1[2]	−7.04	L5	−6.86	L1[2]	−7.01	L7	−6.56	L1[2]	−6.68
L4	−6.94	L0[2]	−7.11	L4	−6.88	L0[2]	−7.04	L6	−6.57	L0[2]	−6.69
L3	−7.22	L0[3]	−7.16	L3	−7.22	L0[3]	−7.16	L3	−7.21	L0[3]	−7.16
L2	−7.45	L2[1]	−7.61	L2	−7.46	L2[1]	−7.61	L2	−7.46	L2[1]	−7.61
L1	−7.68	L1[1]	−7.84	L1	−7.69	L1[1]	−7.84	L1	−7.69	L1[1]	−7.84
L0	−7.76	L0[1]	−7.92	L0	−7.76	L0[1]	−7.92	L0	−7.76	L0[1]	−7.92
H0	−8.26	H0[3]	−8.21	H0	−8.26	H0[3]	−8.21	H0	−8.25	H0[3]	−8.21
H1	−8.70	H0[2]	−8.90	H1	−8.60	H0[2]	−8.78	H1	−8.51	H0[2]	−8.64
H2	−8.91	H1[3]	−8.85	H2	−8.90	H1[3]	−8.85	H3	−8.89	H1[3]	−8.85
H3	−8.99	H1[2]	−9.16	H3	−8.94	H1[2]	−9.09	H2	−8.57	H1[2]	−8.69

<sup>a</sup>Hn[m] and Ln[m] denote the respective HOMO−n and LUMO+n orbitals localized on fragment m (m = 1, 2, 3 for pyrrole–fullerene, diaryl-based porphyrin, and  $\beta$ -carotenoid polyene, respectively).

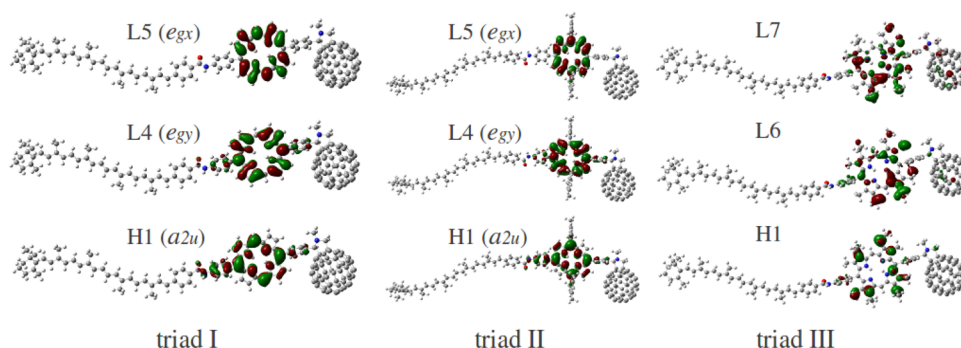


**Figure 3.** Isosurfaces for the HOMO–1, LUMO+4, and LUMO+5 of triads I and II as well as the HOMO–1, LUMO+6, and LUMO+7 of triad III.

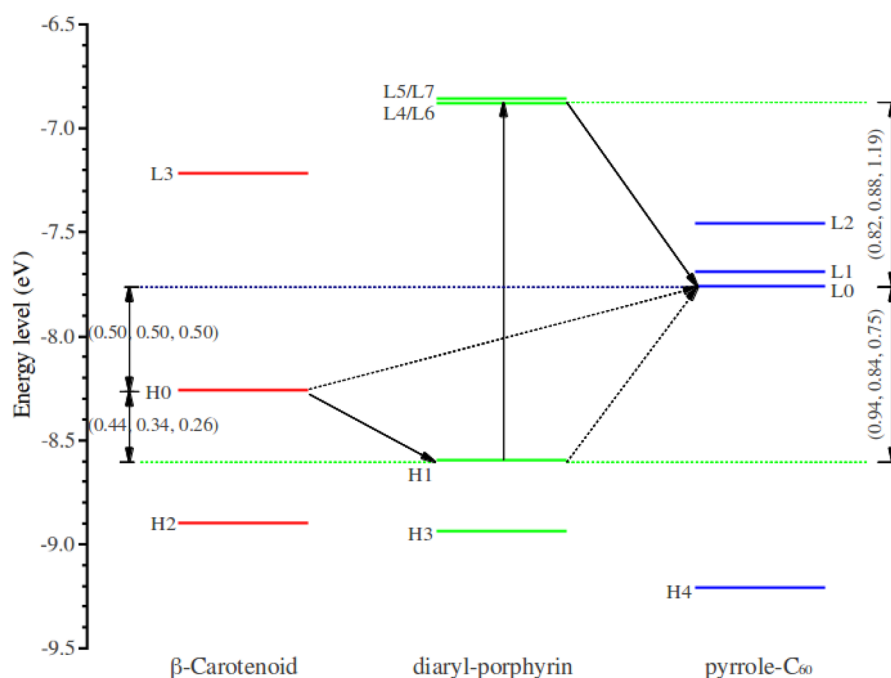


**Figure 4.** Energy diagram for the triads.  $H_n$  and  $L_n$  denote HOMO– $n$  and LUMO+ $n$ , respectively.

nearly degenerate LUMO+3 and LUMO+4 of fullerene. They are increased by ca. 0.1 eV when the triads form, yet with the ordering unchanged. As a result, the LUMO and LUMO+1 of porphyrin correspond to the LUMO+4 and LUMO+5 of triads I and II, whereas to the LUMO+6 and LUMO+7 of triad III. As seen from Figure 3, the isosurfaces of the HOMO, LUMO, and LUMO+1 of porphyrin are indeed very much the same in triads I and II but are very different from those in triad III. Roughly speaking, porphyrin possesses a local  $D_{4h}$  symmetry. The HOMO of porphyrin in triads I and II can be ascribed to the  $a_{2u}$  irreducible representation, whereas that in triad III belongs to  $a_{1u}$ . The former is densely populated on the porphyrin ring and has lobes at the meso positions, whereas the latter is distributed substantially on the alkyl chains and has nodes at the meso positions, indicating that the alkyl chains pull the electron density away from the porphyrin ring. A similar situation also occurs to the LUMO and LUMO+1, which arise from the splitting of the doubly degenerate  $e_g$  orbital of the isolated porphyrin. For comparison, the HOMO–1, HOMO, and LUMO of carotenoid do not change much when the triads form. It looks like that they behave as spectators. In sum, although covalently bonded, the interfragment couplings for the three triads are similarly rather weak insofar as the frontier

orbitals are concerned, such that the ground-state electronic structure of the triads can well be understood in terms of the fragment moieties, precisely in the merit of FLMO.<sup>17,24</sup> These findings are in line with the previous results.<sup>14–16</sup>

Because the energy differences between the virtual and occupied orbitals represent the independent particle approximation (IPA) to the true excitation energies, some insights on the excited states can already be gained at this stage. First of all, the low-lying excited states, in the range between 0.5 and 2.5 eV, should be very similar for the three triads, provided that the frontier orbitals shown in Table 2 make the major contributions. Second, the HOMO  $\rightarrow$  LUMO transition of the porphyrin unit (denoted as  $C^{-1}P-C_{60}$ ), which is 1.76 eV for triad I, 1.72 eV for triad II, and 1.94 eV for triad III, corresponds obviously to the experimental laser absorption at 650 nm (1.91 eV) or 590 nm (2.10 eV).<sup>13</sup> Because the now occupied LUMO of porphyrin is higher than the LUMO of fullerene, a charge transfer from porphyrin to fullerene can take place, leading to  $C-P^+-C_{60}^{\bullet-}$ . The highly conjugated bonds of fullerene form an enclosed cage with a radius as large as 3.45 Å, such that the extra charge can well be stabilized. Energetically, the  $C-P^+-C_{60}^{\bullet-}$  state is lower (higher) than  $C^{-1}P-C_{60}$  ( $C-P-C_{60}$ ) by 0.82 (0.94), 0.88 (0.84), and 1.19

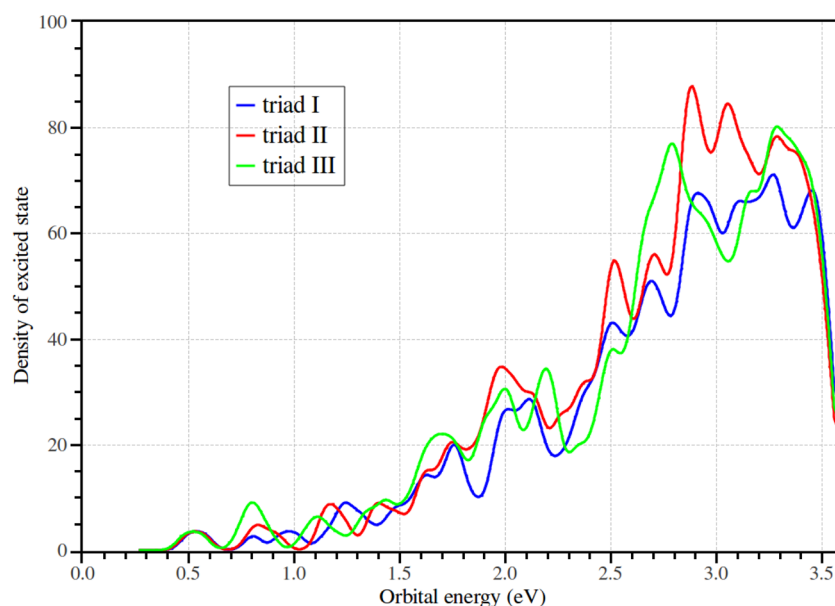


**Figure 5.** Gaussian broadened [full width at half-maximum (fwhm) = 0.1 eV] densities of excited states for the triads.

(0.75) eV for triads I to III, respectively. If the charge recombination of  $C-P^{*+}-C_{60}^{\bullet-}$  to the ground-state  $C-P-C_{60}$  takes place in the Marcus inverted region, the rate ( $k_1$ ) of this charge recombination would increase going from triads I to III (i.e.,  $k_1^I < k_1^{II} < k_1^{III}$ ). On the other hand, the HOMO of carotenoid is higher than the HOMO of porphyrin which now has a vacancy, such that the  $C-P^{*+}-C_{60}^{\bullet-}$  state can evolve eventually to  $C^{*+}-P-C_{60}^{\bullet-}$ , which has a large dipole moment and long lifetime and can hence store the converted energy.<sup>11–13</sup> Energetically, the  $C^{*+}-P-C_{60}^{\bullet-}$  state is lower than  $C-P^{*+}-C_{60}^{\bullet-}$  by 0.43, 0.34, and 0.26 eV for triads I to III, respectively. Therefore, the rate ( $k_2$ ) going from  $C-P^{*+}-C_{60}^{\bullet-}$  to  $C^{*+}-P-C_{60}^{\bullet-}$ , which is in the Marcus normal region, should decrease going from triad I to III (i.e.,  $k_2^I > k_2^{II} > k_2^{III}$ ). As a result, the quantum yield ( $\propto k_2/(k_1 + k_2)$ ) for  $C^{*+}-P-C_{60}^{\bullet-}$  decreases going from triad I to III. A schematic illustration of such dynamical processes is shown in Figure 4. Although the above arguments have been based solely on the energy levels without accounting for, e.g., vibronic and solvation effects, they are in line with the experimental results.<sup>13</sup>

**4.2. Low-Lying Excited States.** To cover the visible part (1.55–3.10 eV) of the solar spectrum, we calculated all the excited states of energies below 3.55 eV, which amount to 320, 370, and 355 states for triads I to III, respectively. The Gaussian broadened densities of excited states (DOES) are plotted in Figure 5. In line with the DOS shown in Figure 2, the DOES of triads I and II are rather similar to each other but are markedly different from that of triad III. The states may be grouped into three types (Table 3), i.e., local excitation (LE), charge transfer (CT), and collective excitation (CE, i.e., heavy mixture of intra- and interfragment transitions without a dominant component). Among the LE states below 2.1 eV, there exist only 2, 1, and 1 states that are localized on porphyrin in triads I to III, respectively (Table 4). Such states for triads I and II are actually “contaminated” by porphyrin  $\rightarrow$  fullerene or carotenoid  $\rightarrow$  porphyrin CTs. Due to such mixings, their energies become higher than the previous IPA estimates by 0.25 and 0.15 eV for triads I/II and III, respectively. Another obvious feature is that triads II and III have more CT states than triad I, especially from porphyrin or carotenoid to fullerene. It appears that

**Table 3. Characterization of the Calculated Excited States of Energy below 3.55 eV<sup>a</sup>**

type	fragment transition (%)	triad I	triad II	triad III
LE	1 $\rightarrow$ 1 ( $\geq 80\%$ )	42	45	48
	2 $\rightarrow$ 2 ( $\geq 80\%$ )	6	13	17
	3 $\rightarrow$ 3 ( $\geq 80\%$ )	3	3	1
	1 $\rightarrow$ 1 (65–80%)	16	12	11
	2 $\rightarrow$ 2 (65–80%)	6	6	3
	3 $\rightarrow$ 3 (65–80%)	5	7	4
sum		78	86	84
CT	2 $\rightarrow$ 1 ( $\geq 80\%$ )	40	72	77
	3 $\rightarrow$ 1 ( $\geq 80\%$ )	40	46	42
	1 $\rightarrow$ 3 ( $\geq 80\%$ )	22	18	22
	1 $\rightarrow$ 2 ( $\geq 80\%$ )	12	10	8
	2 $\rightarrow$ 3 ( $\geq 80\%$ )	8	16	24
	3 $\rightarrow$ 2 ( $\geq 80\%$ )	10	7	8
	2 $\rightarrow$ 1 (65–80%)	6	10	7
	3 $\rightarrow$ 1 (65–80%)	6	3	14
	1 $\rightarrow$ 3 (65–80%)	0	6	1
	1 $\rightarrow$ 2 (65–80%)	1	2	3
	2 $\rightarrow$ 3 (65–80%)	6	6	3
	3 $\rightarrow$ 2 (65–80%)	5	12	4
sum		156	208	213
CE	1 $\rightarrow$ 1 (<65%)	11	16	12
	2 $\rightarrow$ 2 (<65%)	11	11	9
	3 $\rightarrow$ 3 (<65%)	8	5	11
	2 $\rightarrow$ 1 (<65%)	33	18	17
	3 $\rightarrow$ 1 (<65%)	9	15	2
	1 $\rightarrow$ 3 (<65%)	2	0	2
	1 $\rightarrow$ 2 (<65%)	2	1	1
	2 $\rightarrow$ 3 (<65%)	7	6	2
	3 $\rightarrow$ 2 (<65%)	3	4	2
sum		86	76	58
total		320	370	355

<sup>a</sup>LE: local excitation. CT: charge transfer. CE: collective excitation (i.e., heavy mixture of intra- and interfragment transitions without a leading term larger than 65%). Fragments 1, 2, and 3 refer to pyrrole–fullerene, diarylporphyrin, and  $\beta$ -carotenoid polyene, respectively.



**Table 4.** Excitation Energies ( $T_v \leq 2.1$  eV), Oscillator Strengths ( $f$ , au), and Fragment/MO Compositions of the States Localized on Porphyrin<sup>a</sup>

triad	$T_v$	$f$	fragment transition (%)	MO transition (%)
I	2.01	0.008	2 → 2(51), 3 → 2(44)	H1[2] → L5[2](33), H2[3] → L5[2](31), H3[2] → L4[2](13)
	2.12	0.057	2 → 2(67), 2 → 1(12)	H1[2] → L4[2](23), H1[2] → L5[2](19), H3[2] → L4[2](14)
II	1.96 (1.91) <sup>b</sup>	0.029	2 → 2(71), 2 → 1(18)	H1[2] → L5[2](30), H1[2] → L4[2](23), H3[2] → L4[2](15), H1[2] → L7[1](14)
III	2.09	0.001	2 → 2(98)	H1[2] → L7[2,1](40), H2[2] → L6[2](36), H1[2] → L8[1,2](13)

<sup>a</sup>Hn[m] and Ln[m] denote the respective HOMO- $n$  and LUMO+ $n$  orbitals localized on fragment  $m$  ( $m = 1, 2, 3$  for pyrrole–fullerene, diaryl-based porphyrin, and  $\beta$ -carotenoid polyene, respectively). <sup>b</sup>Experimental value measured in 2-methyltetrahydrofuran.<sup>13</sup>

**Table 5.** Excitation Energies ( $T_v$ , eV), Oscillator Strengths ( $f$ , au), and Fragment/MO Compositions of the Bright Excited States of Triad I<sup>a</sup>

no. <sup>b</sup>	$T_v$	$f$	type	fragment transition (%) <sup>c</sup>	MO transition (%) <sup>c</sup>
1	1.32 [3.93] <sup>d</sup>	0.132 [0.020] <sup>d</sup>	CT	3 → 2(97)	H0 → L4(96)
2	1.47 [1.99] <sup>d</sup>	0.302 [0.200] <sup>d</sup>	CT	2 → 3(95)	H1 → L3(95)
3	1.61 (1.7) <sup>e</sup>	2.621	LE	3 → 3(90)	H0 → L3(48), H0 → L9(23), H2 → L3(14)
4	1.83 (1.7) <sup>e</sup>	1.877	LE	3 → 3(90)	H2 → L3(44), H0 → L9(28), H0 → L3(14)
5	2.42 (2.3) <sup>e</sup>	0.219	LE	3 → 3(89)	H2 → L9(52), H0 → L11(19), H9 → L3(15)
6	2.65	0.104	CE	2 → 2(35), 2 → 1(34), 3 → 2(25)	H9 → L4(53), H20 → L1(20), H3 → L10(14)
7	2.92 (2.8) <sup>e</sup>	0.203	CE	2 → 2(54), 1 → 1(20)	H12 → L4(14), H28 → L1(12), H13 → L4(13)
8	2.98	0.099	LE	2 → 2(84)	H12 → L5(24), H3 → L4(10)
9	3.09	0.150	CE	2 → 1(47), 2 → 2(25), 2 → 3(11)	H1 → L16(31), H1 → L15(17)
10	3.10	0.134	CE	2 → 1(54), 2 → 3(14), 3 → 3(13), 2 → 2(11)	H10 → L7(34), H9 → L9(20), H1 → L16(16)
11	3.11	0.161	CE	2 → 3(38), 2 → 2(19), 2 → 1(16), 3 → 3(15)	H9 → L9(30), H12 → L6(17)
12	3.16	0.149	CE	2 → 2(65), 2 → 1(14)	H13 → L5(17), H14 → L5(16), H12 → L5(11), H1 → L18(10)
13	3.19 (3.2) <sup>e</sup>	0.209	CE	2 → 2(33), 2 → 1(27), 3 → 2(18)	H35 → L0(19), H1 → L16(17)
14	3.51	0.113	CE	2 → 2(32), 3 → 3(25), 1 → 1(13), 3 → 2(11)	H14 → L9(20), H15 → L7(10)
15	3.55	0.105	CE	3 → 3(63), 3 → 2(23)	H8 → L11(21)

<sup>a</sup>LE: local excitation. CT: charge transfer. CE: collective excitation. Hn = HOMO+ $n$ ; Ln = LUMO+ $n$ . <sup>b</sup>Only states with  $f \geq 0.09$  au are listed. <sup>c</sup>Only contributions larger than 10% are listed. <sup>d</sup>Results by the maximum occupation method. The overlaps between the excited and ground states are ca. 0.02. <sup>e</sup>Real-time TD-DFT simulations with a resolution of 0.15 eV.<sup>15</sup>

**Table 6.** Excitation Energies ( $T_v$ , eV), Oscillator Strengths ( $f$ , au), and Fragment/MO Compositions of the Bright Excited States of Triad II<sup>a</sup>

no. <sup>b</sup>	$T_v$	$f$	type	fragment transition (%) <sup>c</sup>	MO transition (%) <sup>c</sup>
1	1.37 [4.94] <sup>d</sup>	0.201 [0.017] <sup>d</sup>	CT	3 → 2(92)	H0 → L4(92)
2	1.60	2.722	LE	3 → 3(91)	H0 → L3(50), H0 → L9(23), H2 → L3(14)
3	1.82	1.845	LE	3 → 3(92)	H2 → L3(43), H0 → L9(28), H0 → L3(14)
4	2.41 (2.42) <sup>e</sup>	0.095	CE	2 → 3(61), 3 → 3(36)	H12 → L3(58), H2 → L9(22)
5	2.41 (2.42) <sup>e</sup>	0.136	CE	3 → 3(50), 2 → 3(44)	H12 → L3(43), H2 → L9(30), H0 → L11(11)
6	2.66 (2.56) <sup>e</sup>	0.119	CE	2 → 2(49), 3 → 2(38)	H9 → L4(77)
7	2.68 (2.71) <sup>e</sup>	0.097	CT	2 → 3(79)	H1 → L11(86)
8	2.84 (2.97) <sup>e</sup>	0.109	CE	2 → 2(47), 1 → 2(36)	H15 → L4(60)
9	2.87 (2.97) <sup>e</sup>	0.209	LE	2 → 2(70), 1 → 2(10)	H15 → L4(10), H14 → L5(11)
10	2.92 (3.10) <sup>e</sup>	0.187	CE	2 → 2(44), 3 → 3(16), 1 → 2(14)	H17 → L4(16), H0 → L20(11), H8 → L9(10)
11	3.05 (3.10) <sup>e</sup>	0.216	CE	2 → 1(31), 2 → 2(26), 3 → 2(18)	H11 → L8(18), H18 → L4(14)
12	3.10 (3.10) <sup>e</sup>	0.132	CE	2 → 2(55), 2 → 3(23)	H1 → L15(26)
13	3.12	0.278	CE	2 → 1(44), 2 → 2(34), 2 → 3(10)	H16 → L7(29), H16 → L5(11)
14	3.13	0.219	CE	2 → 1(51), 2 → 2(32)	H16 → L7(48)
15	3.31	0.100	CE	2 → 2(54), 1 → 3(15), 3 → 2(13)	H19 → L5(32), H20 → L5(18), H17 → L9(16)
16	3.54	0.155	CE	3 → 3(60), 3 → 2(19), 2 → 3(13)	H8 → L11(32), H18 → L9(12)

<sup>a</sup>LE: local excitation. CT: charge transfer. CE: collective excitation. Hn = HOMO+ $n$ ; Ln = LUMO+ $n$ . <sup>b</sup>Only states with  $f \geq 0.09$  au are listed. <sup>c</sup>Only contributions larger than 10% are listed. <sup>d</sup>Results by the maximum occupation method. The overlap between the excited and ground states is ca. 0.02. <sup>e</sup>Experimental values measured in 2-methyltetrahydrofuran.<sup>13</sup>

chemical substitutions of porphyrin facilitate CTs that are relevant for the conversion of solar energy into electric potential energy. Yet, most of the CT states are dark. On the other hand, due to the 1/R failure, the ALDA/TD-DFT

energies for the long-range CT states are just the orbital energy differences, which are severe underestimates of the true excitation energies. Such states should hence be removed from the calculations. However, we decide not to do this for



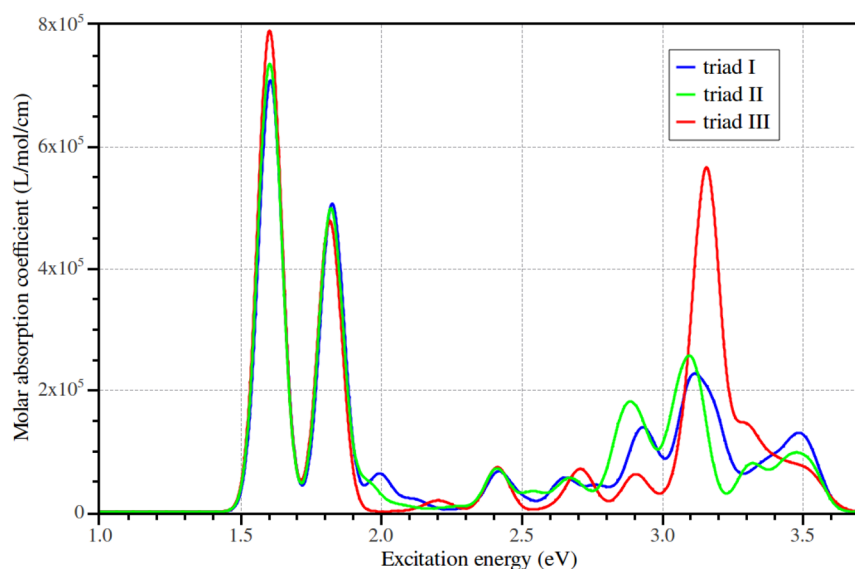


Figure 6. Optical absorption spectra of the three triads.

Table 7. Excitation Energies ( $T_v$ , eV), Oscillator Strengths ( $f$ , au), and Fragment/MO Compositions of the Bright Excited States of Triad III<sup>a</sup>

no. <sup>b</sup>	$T_v$	$f$	type	fragment transition (%) <sup>c</sup>	MO transition (%) <sup>c</sup>
1	1.60	2.932	LE	3 → 3(90)	H0 → L3(57), H0 → L9(23), H3 → L3(16)
2	1.82	1.772	LE	3 → 3(86)	H3 → L3(44), H0 → L9(30), H3 → L3(15)
3	2.42 (2.43) <sup>d</sup>	0.255	LE	3 → 3(83)	H3 → L9(56), H11 → L3(19), H0 → L11(18)
4	2.71 (2.56) <sup>d</sup>	0.091	CE	2 → 2(41), 2 → 1(29)	H27 → L0(30), H5 → L7(14)
5	2.90 (2.73) <sup>d</sup>	0.079	CE	1 → 3(32), 3 → 3(28), 2 → 3(17)	H10 → L9(35), H10 → L9(34), H0 → L19(16)
6	3.07 (3.01) <sup>d</sup>	0.091	CE	2 → 2(41), 2 → 1(29)	H1 → L18(87)
7	3.11 (3.01) <sup>d</sup>	0.334	LE	2 → 2(81), 2 → 1(11)	H2 → L18(47)
8	3.14	0.266	LE	1 → 1(87)	H31 → L2(26), H33 → L1(16)
9	3.15	0.281	CE	2 → 2(57), 1 → 1(22), 2 → 1(19)	H2 → L18(34), H13 → L8(12)
10	3.16	0.122	CT	1 → 2(82), 2 → 2(12)	H14 → L6(80)
11	3.17	0.439	CE	1 → 2(52), 2 → 2(26), 1 → 1(17)	H14 → L7(47)
12	3.17	0.614	CE	2 → 2(35), 1 → 2(34), 1 → 1(25)	H14 → L7(34)
13	3.28	0.093	LE	2 → 2(72), 2 → 1(14), 1 → 1(11)	H13 → L6(51), H16 → L5(13)
14	3.31	0.210	LE	2 → 2(82)	H2 → L21(72)
15	3.40	0.153	LE	2 → 2(94)	H2 → L23(68)

<sup>a</sup>LE: local excitation. CT: charge transfer. CE: collective excitation.  $Hn$  = HOMO+ $n$ ;  $Ln$  = LUMO+ $n$ . <sup>b</sup>Only states with  $f \geq 0.09$  au are listed. <sup>c</sup>Only contributions larger than 10% are listed. <sup>d</sup>Experimental values measured in toluene.<sup>11</sup>

two reasons. First, the number of CT pairs (see CT transitions of more than 80% in Table 3) is only ca. 1% of the total effective p–h pairs ( $N_{\text{eff}}$  ( $\eta = 6$ ) in Table 2), such that elimination of such pairs from the p–h space does not gain much efficiency. In case a long-range corrected functional is used, such CT states would well be described. Because the present FLMO-TD-DFT with pure and hybrid functionals differs only in the prefactor but not in the scaling, the inclusion of such CT pairs in the present calculations can be viewed as an *aforehand* illustration of the efficacy of the FLMO-LC-TD-DFT to be developed in the future. Second and more important, elimination of such CT pairs might significantly affect the collective excitations. Instead, the aforementioned mom (14) was applied to recalculate the bright CT states self-consistently. As seen from Table 5, triad I has 2 pure CT transitions between carotenoid and porphyrin, which are blue-shifted by 2.6 and 0.5 eV, respectively, by the mom calculations. As a result, the ordering of these two states gets reversed. Close inspections reveal that, for the CT state stemming from the

HOMO (carotenoid) to LUMO+4 (porphyrin) transition, the MOs dominated by the positively charged carotenoid become lower by 0.3–0.4 eV, whereas those dominated by the negatively charged porphyrin become higher by 1.2–1.4 eV than the ground-state counterparts. Due to interplay with the negatively charged porphyrin, the MOs dominated by fullerene also become higher by ca. 1 eV than the ground-state counterparts. The opposite trend occurs to the CT state arising from the HOMO–1 (porphyrin) to LUMO+3 (carotenoid): The MOs dominated by the negatively charged carotenoid become higher by ca. 1 eV, whereas those dominated by the positively charged carotenoid become lower by 0.5–0.7 than the ground-state counterparts. Concomitantly, the MOs dominated by fullerene become also lower by ca. 0.3 eV than the ground-state counterparts. As the overall changes in the energy levels of carotenoid and porphyrin are comparable for these two CT states, it is the substantially large increases in the energy levels of fullerene that are mainly responsible for the larger blue shift of the HOMO → LUMO+4

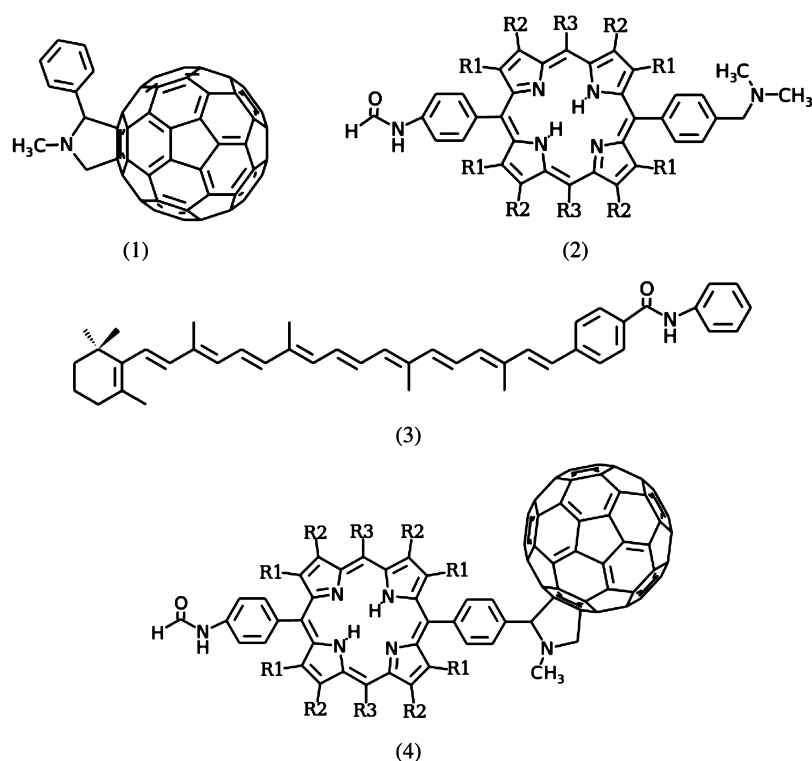


**Figure 7.** Structures for the capped fragments and dyads. (1) pyrrole–fullerene; (2) diarylporphyrin [dyad I:  $R_1 = R_2 = R_3 = H$ ; dyad II:  $R_1 = CH_3$ ,  $R_2 = CH_2CH_3$ ,  $R_3 = H$ ; dyad III:  $R_1 = R_2 = H$ ,  $R_3 = Ph(CH_3)_3$ ]; (3)  $\beta$ -carotenoid polyene; (4) dyad.

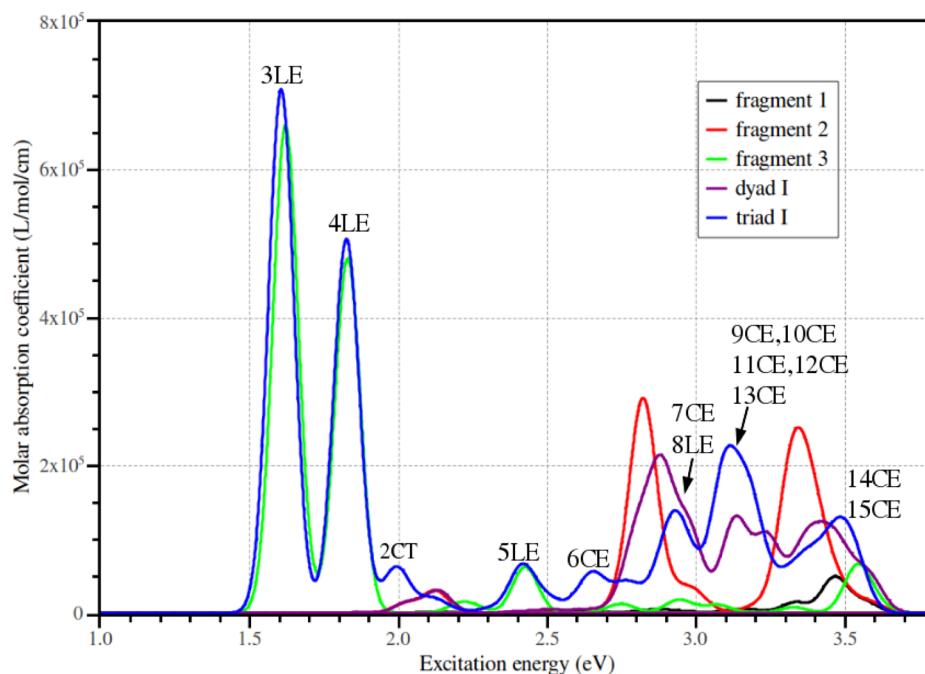


**Figure 8.** Optical absorption spectra for the fragments and dyad in triad I. LE: local excitation. CT: charge transfer (NB: 2CT from the mom calculation). CE: collective excitation (Table 5).

CT state. A similar situation occurs also to the HOMO  $\rightarrow$  LUMO+4 CT state of triad II (Table 6). However, the CT state of triad II (no. 7 in Table 6) arising from HOMO–1 (porphyrin) to LUMO+11 (carotenoid) is not a pure CT state and cannot be calculated by the mom. It should be mentioned here that the original MOM (12)<sup>39</sup> fails completely for the

present systems. This is the very reason why it is revised to the present mom (14).

From now on, we focus on the non-CT bright states, which are plotted in Figure 6 for a cross comparison of the three triads. As expected, the spectral patterns of the three triads are very similar below 2.5 eV. The two sharp and intense peaks located at 1.6 and 1.8 eV correspond to local excitations of

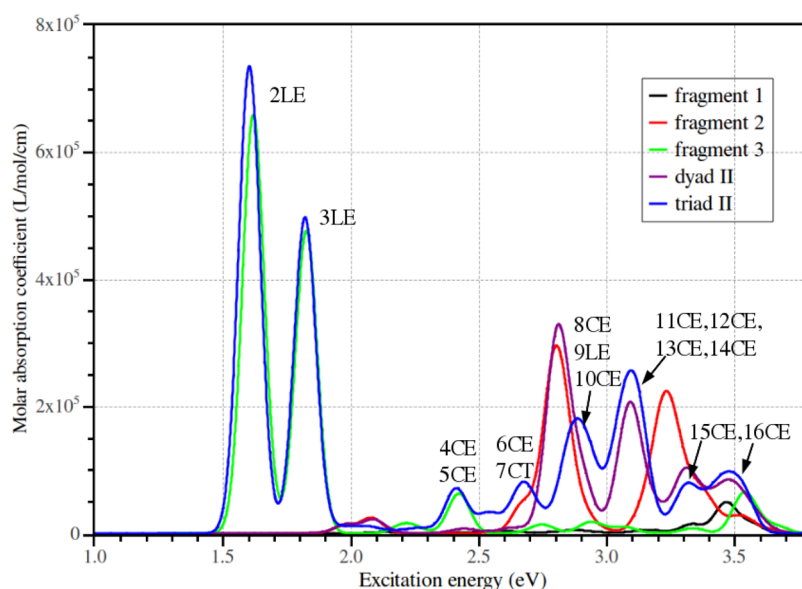


**Figure 9.** Optical absorption spectra for the fragments and dyad in triad II. LE: local excitation. CT: charge transfer. CE: collective excitation (Table 6).

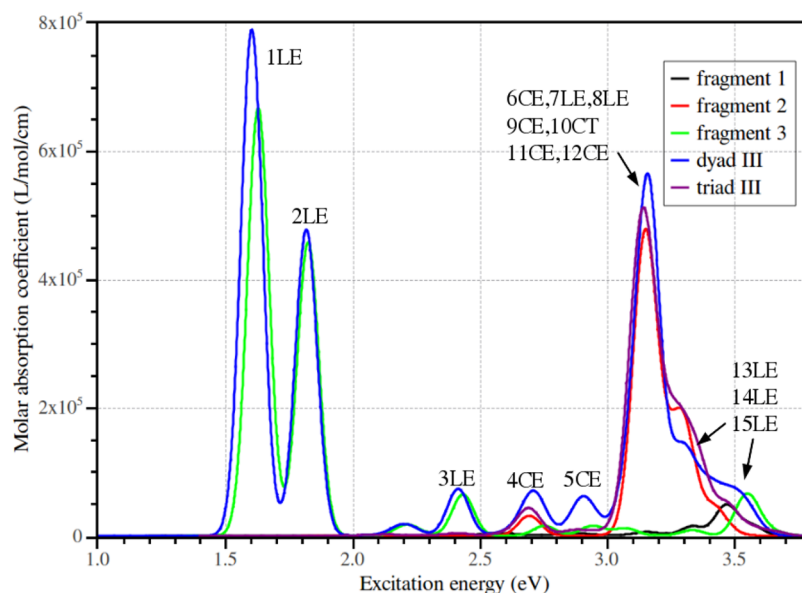


**Figure 10.** Optical absorption spectra for the fragments and dyad in triad III. LE: local excitation. CT: charge transfer. CE: collective excitation (Table 7).

carotenoid for all the three triads (Tables 5–7). The weak peak at 2.4 eV is also such a local excitation for triads I and III. However, for triad II, it consists of two nearly degenerate states that arise from collective excitations involving the carotenoid and porphyrin units. More specifically, they are heavy mixtures of the carotenoid-local and carotenoid  $\rightarrow$  porphyrin CT excitations. The spectra of triads I and II remain similar in the B-band region (2.5–3.5 eV), but that of triad III looks quite different, especially in the region above 3.0 eV. The weak peak around 2.7 eV arises from the collective porphyrin-local and porphyrin  $\rightarrow$  fullerene CT excitations for triads I and III. In contrast, this peak for triad II again consists of two nearly degenerate states, one of which arises from the collective porphyrin-local and carotenoid  $\rightarrow$  porphyrin CT excitations, whereas the other is dominated by the porphyrin  $\rightarrow$  carotenoid CT. The next peak at 2.9 eV for triads I and II can best be

characterized as collective excitations but with the local excitation of porphyrin as the leading term. This peak consists of two and three states for triads I and II, respectively. Yet, this peak for triad III is a single state composed of carotenoid-local and (fullerene, porphyrin)  $\rightarrow$  carotenoid back CT excitations. The peak between 3.1 and 3.2 eV consists of five and four states for triads I and II, respectively, which are collective excitations involving all the three units. In contrast, this peak for triad III is composed of four collective, two local, and one back-CT (i.e., fullerene  $\rightarrow$  porphyrin) states, all of which involve only the porphyrin and fullerene units. Overall, the peaks between 2.6 and 3.2 eV for triad II are lower in energy and more intense in amplitude than those for triad I. Therefore, the *meso*-aryl substitutions of porphyrin enhance the collective excitations. The opposite is true for the  $\beta$ -alkyl substitutions. The peak at 3.5 eV for triad I contains two collective excitations involving all

the three units, which is split into two peaks at 3.3 and 3.5 eV for triad II. For comparison, this peak for triad III consists of three local excitations on porphyrin. In short, the states of triad III above 3.0 eV have no contributions from carotenoid, whereas those of triads I and II involve heavy carotenoid contributions, through the occupied and/or virtual orbitals of pure carotenoid character or those of mixed carotenoid and porphyrin components (e.g., HOMO–8 and HOMO–9). Therefore, the interfragment couplings are stronger for triads I and II than for triad III as far as the high-lying states are concerned. Note that this does not conflict with the previous statement that the interfragment couplings for the three triads are similarly rather weak, because the focus there was on the low-lying states (below 2.5 eV) involving the frontier orbitals (Table 2). Finally, the present results are grossly in good agreement with the available experimental<sup>7,13</sup> and theoretical<sup>15</sup> values.

At variance with the above top-down decomposition of the calculated excited states, a bottom-up analysis can also be made. For this purpose, we carried out the corresponding states of the capped fragments and dyads shown in Figure 7. The results are plotted in Figures 8–10. Without going into details, several major observations can be made here. First, the carotenoid unit has two intense and one weak absorptions located at 1.60, 1.85, and 2.42 eV. The basic (*meso*-aryl substituted) porphyrin unit has two peaks at 2.83 (2.80) and 3.35 (3.25) eV. The former is largely suppressed and red-shifted to 2.70 eV, whereas the latter is red-shifted to 3.15 eV followed by a shoulder at 3.30 eV for the  $\beta$ -alkyl substituted porphyrin. The fullerene unit has only one weak absorption at 3.45 eV. When the porphyrin and fullerene form the dyad, a simple superposition occurs to the case of dyad III, whereas in the case of dyad I (II), the peak of porphyrin around 3.3 eV is split into two peaks at 3.15 (3.10) and 3.25 (3.35) eV due to mixing in the fullerene component. Going from the dyad to triad, the states localized on carotenoid still survive for all the cases. Again, little changes occur to triad III in the region above 3.0 eV, in contrast with triads I and II. Overall, triads I and II have more features than triad III in the region above 2.5 eV. All these are in accordance with the previous findings from the top-down analysis. This exercise reveals that it is generally an effective means for fabricating single molecular light-harvesting systems by assembling subsystems of well-defined optical properties.

## 5. CONCLUSION

Comprehensive theoretical investigations have been carried out on the photoexcitation of the C–P–C<sub>60</sub> triads that are of interest for new generation solar devices. Although the systems have a large number of low-lying excited states in the visible part of the solar spectrum, the results can readily be analyzed in terms of the underlying idea of “from fragments to molecule”. That is, local, delocalized, and charge-transfer kinds of excitations emerge in a natural manner. On the basis of such analysis, it is deduced that both triads I and II tend to have higher quantum yields for the charge-separated-state C<sup>•+</sup>–P–C<sub>60</sub><sup>•–</sup> than triad III, primarily due to the steric repulsion between the  $\beta$ -alkyl substitutions of porphyrin in triad III, which results in a different local symmetry from that of triad I/II. The simulated optical absorption spectra are grossly in good agreement with experimental observations. Loosely speaking, the spectra of the three triads can be regarded as simple superpositions of the fragment units. Yet, some subtleties still exist. Though the Q-bands (below 2.5 eV) of the three triads

are very similar, the B-band (2.5–3.5 eV) of triad III is quite different from those of I and II: The bright states of triad III above 3.0 eV have no contributions from carotenoid, whereas those of triads I and II involve heavy carotenoid contributions, through the occupied and/or virtual orbitals of pure carotenoid character or those of mixed carotenoid and porphyrin components. On the other hand, the peaks of triad II between 2.6 and 3.2 eV are clearly lower in energy and more intense in amplitude than those of triad I. That is, the *meso*-aryl substitutions of porphyrin tend to enhance the collective excitations. These findings enrich the structure–property relations. Nevertheless, conformational, vibronic, and solvation effects have to be further taken into account for more decisive assessments. Work along these directions, following the strategies outlined before,<sup>48,49</sup> is being undertaken at our laboratory. As a supplement to TD-DFT, a self-consistent maximum occupation method is proposed for calculating excited states variationally. Its potential remains to be revealed by more extensive applications.

## AUTHOR INFORMATION

### Corresponding Author

\*W. Liu: e-mail, liuwjbd@f@gmail.com.

### Notes

The authors declare no competing financial interest.

## ACKNOWLEDGMENTS

This work was supported by the NSFC (Project Nos. 21033001, 21273011, and 21290192).

## REFERENCES

- (1) Lewis, N. S.; Nocera, D. G. *Proc. Natl. Acad. Sci. U. S. A.* **2006**, *103*, 15729–15735.
- (2) Cheng, Y. J.; Yang, S. H.; Hsu, C. S. *Chem. Rev.* **2009**, *109*, 5868–5923.
- (3) Clarke, T. M.; Durrant, J. R. *Chem. Rev.* **2010**, *110*, 6736–6767.
- (4) Lin, Y.; Li, Y.; Zhan, X. *Chem. Soc. Rev.* **2012**, *41*, 4245–4272.
- (5) Mishra, A.; Bäuerle, P. *Angew. Chem., Int. Ed.* **2012**, *51*, 2020–2067.
- (6) Segura, J. L.; Martín, N.; Guldi, D. M. *Chem. Soc. Rev.* **2005**, *34*, 31–47.
- (7) Green, M. A.; Emery, K.; Hishikawa, Y.; Warta, W.; Dunlop, E. D. *Prog. Photovolt. Res. Appl.* **2013**, *21*, 1–11.
- (8) Roncali, J. *Adv. Energy Mater.* **2011**, *1*, 147–160.
- (9) Wang, M.; Wudl, F. *J. Mater. Chem.* **2012**, *22*, 24297–24314.
- (10) Panda, M. K.; Ladomenou, K.; Coutsolelos, A. G. *Coord. Chem. Rev.* **2012**, *256*, 2601–2627.
- (11) Liddell, P. A.; Kuciauskas, D.; Sumida, J. P.; Nash, B.; Nguyen, D.; Moore, A. L.; Moore, T. A.; Gust, D. *J. Am. Chem. Soc.* **1997**, *119*, 1400–1405.
- (12) Carbonera, D.; Valentin, M. D.; Corvaja, C.; Agostini, G.; Giacometti, G.; Liddell, P. A.; Kuciauskas, D.; Moore, A. L.; Moore, T. A.; Gust, D. *J. Am. Chem. Soc.* **1998**, *120*, 4398–4405.
- (13) Kodis, G.; Liddell, P. A.; Moore, A. L.; Moore, T. A.; Gust, D. *J. Phys. Org. Chem.* **2004**, *17*, 724–734.
- (14) Baruah, T.; Pederson, M. R. *J. Chem. Phys.* **2006**, *125*, 164706.
- (15) Spallanzani, N.; Rozzi, C. A.; Varsano, D.; Baruah, T.; Pederson, M. R.; Manghi, F.; Rubio, A. *J. Phys. Chem. B* **2009**, *113*, 5345–5349.
- (16) Baruah, T.; Pederson, M. R. *J. Chem. Theory Comput.* **2009**, *9*, 834–843.
- (17) Wu, F.; Liu, W.; Zhang, Y.; Li, Z. *J. Chem. Theory Comput.* **2011**, *7*, 3643–3660.
- (18) Casida, M. E. Time-dependent Density Functional Response Theory for Molecules. In *Recent Advances in Density Functional Methods*



(Part I); Chong, D. P., Ed.; Recent Advances in Computational Chemistry, Vol. 1; World Scientific: Singapore, 1995; pp 155–192.

(19) Tretiak, S.; Isborn, C. M.; Niklasson, A. M. N.; Challacombe, M. *J. Chem. Phys.* **2009**, *130*, 054111.

(20) Stratmann, R. E.; Scuseria, G. E.; Frisch, M. J. *J. Chem. Phys.* **1998**, *109*, 8218–8224.

(21) Jansík, B.; Høst, S.; Kristensen, K.; Jørgensen, P. *J. Chem. Phys.* **2011**, *134*, 194104.

(22) Høyvik, I.-M.; Jansík, B.; Jørgensen, P. *J. Chem. Theory Comput.* **2012**, *8*, 3137–3146.

(23) Boys, S. F. *Rev. Mod. Phys.* **1960**, *32*, 296–299.

(24) Li, Z.; Li, H.; Suo, B.; Liu, W. *Acc. Chem. Res.*, submitted for publication.

(25) van Gisbergen, S. J. A.; Guerra, C. F.; Baerends, E. J. *J. Comput. Chem.* **2000**, *21*, 1511–1523.

(26) Coriani, S.; Høst, S.; Jansík, B.; Thøgersen, L.; Olsen, J.; Jørgensen, P.; Reine, S.; Pawłowski, F.; Helgaker, T.; Sælek, P. *J. Chem. Phys.* **2007**, *126*, 154108.

(27) Kovyshin, A.; De Angelis, F.; Neugebauer, J. *Phys. Chem. Chem. Phys.* **2012**, *14*, 8608–8619.

(28) Grimme, S. *J. Chem. Phys.* **2013**, *138*, 244104.

(29) Jensen, L.; Autschbach, J.; Schatz, G. C. *J. Chem. Phys.* **2005**, *122*, 224115.

(30) Rocca, D.; Gebauer, R.; Saad, Y.; Baroni, S. *J. Chem. Phys.* **2008**, *128*, 154105.

(31) Dreuw, A.; Head-Gordon, M. *J. Am. Chem. Soc.* **2004**, *126*, 4007–4016.

(32) Gritsenko, O.; Baerends, E. J. *J. Chem. Phys.* **2004**, *121*, 655–660.

(33) Ziegler, T.; Seth, M.; Krykunov, M.; Autschbach, J. *J. Chem. Phys.* **2008**, *129*, 184114.

(34) Iikura, H.; Tsuneda, T.; Yanai, T.; Hirao, K. *J. Chem. Phys.* **2001**, *115*, 3540–3544.

(35) Tawada, Y.; Tsuneda, T.; Yanagisawa, S.; Yanai, T.; Hirao, K. *J. Chem. Phys.* **2004**, *120*, 8425–8433.

(36) Yanai, T.; Tew, D. P.; Handy, N. C. *Chem. Phys. Lett.* **2004**, *393*, 51–57.

(37) Cullen, J.; Krykunov, M.; Ziegler, T. *Chem. Phys.* **2011**, *391*, 11–18.

(38) Ziegler, T.; Krykunov, M.; Cullen, J. *J. Chem. Phys.* **2012**, *136*, 124107.

(39) Gilbert, A. T. B.; Besley, N. A.; Gill, P. M. W. *J. Phys. Chem. A* **2008**, *112*, 13164–13171.

(40) Perdew, J. P.; Burke, K.; Ernzerhof, M. *Phys. Rev. Lett.* **1996**, *77*, 3865–3868.

(41) Lenthe, E. V.; Baerends, E. J. *J. Comput. Chem.* **2003**, *24*, 1142–1156.

(42) Schipper, P. R. T.; Gritsenko, O. V.; van Gisbergen, S. J. A.; Baerends, E. J. *J. Chem. Phys.* **2000**, *112*, 1344–1352.

(43) Vosko, S. H.; Wilk, L.; Nusair, M. *Can. J. Phys.* **1980**, *58*, 1200–1211.

(44) Liu, W.; Hong, G.; Dai, D.; Li, L.; Dolg, M. *Theor. Chem. Acc.* **1997**, *96*, 75–83.

(45) Liu, W.; Wang, F.; Li, L. *J. Theor. Comput. Chem.* **2003**, *2*, 257–272.

(46) Liu, W.; Wang, F.; Li, L. Relativistic Density Functional Theory: The BDF Program Package. In *Recent Advances in Relativistic Molecular Theory*; Hirao, K., Ishikawa, Y., Eds.; Recent Advances in Computational Chemistry; World Scientific: Singapore, 2004; Vol. 5, pp 257–282.

(47) Lu, T.; Chen, F. W. *J. Comput. Chem.* **2012**, *33*, 580–592.

(48) Shuai, Z.; Liu, W.; Liang, W.; Shi, Q.; Chen, H. *Sci. China Chem.* **2013**, *56*, 1258–1262.

(49) Liu, W.; Ma, J. *Sci. China Chem.* **2013**, *56*, 1263–1266.